A&A 562, A12 (2014)
DOI: 10.1051/0004-6361/201322833

Astronomy & Astrophysics

One-zone synchrotron self-Compton model for the core emission of Centaurus A revisited

M. Petropoulou, E. Lefa, S. Dimitrakoudis, and A. Mastichiadis

Department of Physics, University of Athens, Panepistimiopolis, 15783 Zografos, Greece
e-mail: maroulaaki@gmail.com

Received 11 October 2013 / Accepted 3 November 2013

ABSTRACT

Aims. We investigate the role of the second synchrotron self-Compton (SSC) photon generation to the multiwavelength emission from the compact regions of sources that are characterized as misaligned blazars. For this, we focus on the nearest high-energy emitting radio galaxy Centaurus A and we revisit the one-zone SSC model for its core emission.
Methods. We have calculated analytically the peak luminosities of the first and second SSC components by first deriving the steady-state electron distribution in the presence of synchrotron and SSC cooling, and then by using appropriate expressions for the positions of the spectral peaks. We have also tested our analytical results against those derived from a numerical code where the full emissivities and cross-sections were used.
Results. We show that the one-zone SSC model cannot account for the core emission of Centaurus A above a few GeV, where the peak of the second SSC component appears. We thus propose an alternative explanation for the origin of the high-energy ($\gtrsim$0.4 GeV) and TeV emission, where these are attributed to the radiation emitted by a relativistic proton component through photohadronic interactions with the photons produced by the primary leptonic component. We show that the required proton luminosities are not extremely high, i.e. $\sim 10^{43}$ erg/s, provided that the injection spectra are modelled by a power law with a high value of the lower energy cutoff. Finally, we find that the contribution of the core emitting region of Cen A to the observed neutrino and ultra-high-energy cosmic-ray fluxes is negligible.

Key words. radiation mechanisms: non-thermal – gamma rays: general – galaxies: active – galaxies: individual: Centaurus A

1. Introduction

Centaurus A (Cen A) is the nearest radio galaxy to the Earth with a luminosity distance $D_L \simeq 3.7$ Mpc[1] and is, therefore, one of the best laboratories for studying the physics of radio lobes, relativistic outflows, shock formation, and thermal and non-thermal emission mechanisms. Because of its proximity, emission from the extended lobes and jet, as well as from its nucleus, has been detected across the electromagnetic spectrum (see e.g. Israel 1998, for a review). In radio wavelengths it has a Fanaroff and Riley Class I (FRI) morphology (Fanaroff & Riley 1974), while in higher energies (X-rays) it is regarded as a misaligned BL Lac object (Morganti et al. 1992; Chiaberge et al. 2001) in agreement with the unification scheme of active galactic nuclei (AGNe; Padovani & Urry 1990, 1991). Although the angle between the jet axis and our line of sight is large, it is still not well constrained mainly because of the assumptions used in its derivation (see e.g. Hardcastle et al. 2003); it ranges between 15° (Hardcastle et al. 2003) and 50°−80° (Tingay et al. 1998).

Gamma-ray emission (∼0.1−10 GeV) from Cen A has been detected by EGRET (Hartman et al. 1999), but the identification of the γ-ray source with the core was uncertain because of the large positional uncertainties. The recent detection of very high energy (VHE) emission (∼TeV) from the core of Cen A by H.E.S.S. (Aharonian et al. 2009), along with the Fermi satellite observations above 100 MeV from the core (Abdo et al. 2010a) and X-ray data from various telescopes, means that it is now possible to construct a well-sampled spectral energy distribution (SED) for its nuclear emission[2], which requires physical explanation. Whether the HE/VHE core emission originates from very compact or extended regions is still unclear because there is not enough information regarding the variability in the GeV/TeV energy ranges and of the current resolution of γ-ray instruments. This complicates further the attempts to fit the multiwavelength (MW) core emission.

The one-zone synchrotron self-Compton (SSC) model is one of the most popular emission models thanks to its simplicity and to the small number of free parameters. In the past it has been successfully applied to the SEDs of various blazars (see e.g. Ghisellini et al. 1998; Celotti & Ghisellini 2008, for steady-state models and Mastichiadis & Kirk 1997; Böttcher & Chiang 2002, for time-dependent ones). We note, however, that rapid flaring events and recent contamporeneous MW observations of blazars pose problems to homogeneous SSC models (Begelman et al. 2008; Böttcher et al. 2009; Costamante et al. 2009). If FRIs are indeed misaligned BL Lac objects, then one expects that the one-zone SSC model should also apply successfully to their MW emission (see e.g. Abdo et al. 2009b, for M87 and Abdo et al. 2009a, for NGC 1275). We note, however, that alternative emission models have also been proposed

[1] Although there is still considerable debate on its distance (see e.g. Ferrarese et al. 2007; Majaess 2010; Harris et al. 2010), we will adopt this value as a representative one.

[2] High-energy (HE) emission was also detected from the radio lobes of Cen A (Abdo et al. 2010b), while a recent analysis by Yang et al. (2012) shows that this emission extends beyond the radio lobes. However, we will not deal with the lobe emission in the present work.

(e.g. Giannios et al. 2010 for M87). In the case of Centaurus A, it is still the leading interpretation scenario for the core emission, at least below the TeV energy range (Chiaberge et al. 2001; Abdo et al. 2010a; Roustazadeh & Böttcher 2011).

There is, however, a subtle point that must be taken into account when applying one-zone models to FRIs. Because of the large viewing angle, the Doppler factor δ cannot take large values (in most cases $\delta < 5$) in contrast to blazars where typical values are $\delta = 20-30$, while even higher values ($40 < \delta < 80$) appear in the literature (Konopelko et al. 2003; Aleksić et al. 2012). Thus, unless the observed γ-ray luminosity of FRIs is a few orders of magnitude lower than the luminosity of the blazars, the injection power of relativistic radiating electrons must be high enough to account for it[3]. The above implies that in cases where the radius of the emitting source is not very large, higher order SSC photon generations may, in general, contribute to the total SED and are not negligible as in the case of blazars.

In the present work we focus on Cen A as a typical example of a misaligned blazar. We show that the simple homogeneous SSC model cannot fully account for its MW core emission because of the emergence of the second SSC photon generation. We therefore present an alternative scenario where the SED up to the GeV energy range is attributed to SSC emission of primary electrons, while the GeV-TeV emission itself is attributed to photohadronic processes.

The present work is structured as follows. In Sect. 2 we calculate analytically using certain approximations the peak luminosities of the synchrotron and SSC (first and second) components for parameters that are relevant to Cen A; in the same section we test our results against those obtained from a numerical code that employs the full expressions for the cross sections and emissivities of all processes. In Sect. 3 we show the effects that the second SSC component has on the overall one-zone SSC fit of the MW core emission of Cen A. In Sect. 4 we introduce a relativistic proton distribution in addition to the primary electron distribution, and present the resulting leptohadronic fits to the emitted MW spectrum; we also discuss the resulting neutrino and ultra-high-energy cosmic ray emission. Finally, we conclude in Sect. 5 with a discussion of our results.

2. Analytical arguments

The calculation of the steady-state electron distribution in the case of a constant in time power-law injection under the influence of synchrotron and SSC (in the Thomson regime) cooling can be found in Lefa & Mastichiadis (in prep., hereafter LM13). However, in the present section and for reasons of completeness, we derive the analogous solution for monoenergetic electron injection. On the one hand, this choice significantly simplifies our analytical calculations. On the other hand, it is justified since the power-law photon spectrum in the range 10^{13}–10^{15} Hz is very steep and it can therefore be approximated by the synchrotron cutoff emission of a monoenergetic electron distribution.

2.1. Steady state solution for the electron distribution

We assume that electrons are being injected at γ_0 and subsequently cool down as a result of synchrotron and SSC losses. Here we assume that all scatterings between electrons and synchrotron photons occur in the Thomson regime, which is true for parameter values related to the spectral fitting of Cen A (see Sects. 2.2 and 3). The electron distribution cools down to a characteristic Lorentz factor γ_c where the escape timescale ($t_{e,esc}$) equals the energy loss timescale and is given by

$$\gamma_c = \frac{3m_e c}{4\sigma_T t_{e,esc}(u_B + u_s)}, \tag{1}$$

where $t_{e,esc} = R/c$, R is the size of the emitting region, u_B is the magnetic energy density and

$$u_s = m_e c^2 \int_{\epsilon_{min}}^{\epsilon_{max}} d\epsilon\, \epsilon n_s(\epsilon), \tag{2}$$

is the energy density of synchrotron photons. The integration limits in Eq. (2) are $\epsilon_{max} = b\gamma_0^2$ and $\epsilon_{min} = b\gamma_c^2$, where $b = B/B_{cr}$ and $B_{cr} = 4.4 \times 10^{13}$ G. In what follows, all energies that appear in the relations will be normalized with respect to $m_e c^2$, unless stated otherwise. Here we assume that γ_c is much smaller than γ_0, which further implies that the particle escape is less significant than the energy losses in shaping the electron distribution at the particular energy range. Thus, the electron distribution n_e at the steady state is described by the kinetic equation

$$Q(\gamma) = \frac{4}{3m_e c^2}\sigma_T c \frac{\partial}{\partial\gamma}\left[\gamma^2 n_e(\gamma)\,(u_B + u_s)\right], \tag{3}$$

where and $Q(\gamma) = Q_0\delta(\gamma - \gamma_0)$ is the injection rate per unit volume of electrons having Lorentz factors in the range $(\gamma, \gamma + d\gamma)$. Under the δ-function approximation for the synchrotron emissivity, the differential number density of synchrotron photons is given by (see e.g. Mastichiadis & Kirk 1995)

$$n_s(\epsilon) = A_2 \epsilon^{-1/2} n_e\left(\sqrt{\frac{\epsilon}{b}}\right), \tag{4}$$

where

$$A_2 = \frac{2}{3} R\sigma_T u_b b^{-3/2} \tag{5}$$

and u_b is the dimensionless magnetic energy density, i.e. $u_b = u_B/m_e c^2$. Plugging Eqs. (2) and (4) into Eq. (3) we find

$$Q_0\delta(\gamma - \gamma_0) = \frac{4}{3}\sigma_T c \frac{\partial}{\partial\gamma}\left[\gamma^2 n_e(\gamma) G_e\right], \tag{6}$$

where G_e depends on the electron distribution as

$$G_e = \left(u_b + \frac{4}{3}\sigma_T R u_b \int_{\gamma_c}^{\gamma_0} dx\, x^2 n_e(x)\right). \tag{7}$$

An ansatz for the solution n_e of the above integro-differential equation is $n_e(\gamma) = k_e\gamma^{-p}$ with k_e and p being the parameters to be determined. By substituting the above solution into Eq. (6) we find that $p = 2$ and that k_e satisfies the quadratic equation

$$\left(\frac{4}{3}\sigma_T R\, u_b\gamma_0\right)k_e^2 + u_b k_e - \frac{3Q_0}{4\sigma_T c} = 0, \tag{8}$$

with k_e being the positive root

$$k_e = \frac{3}{8\sigma_T R\gamma_0}\left(-1 + \sqrt{1 + \frac{4Q_0 R\gamma_0}{c u_b}}\right). \tag{9}$$

It is more convenient to express k_e in terms of the electron injection compactness ℓ_e^{inj}, which is defined as

$$\ell_e^{inj} = \frac{\sigma_T L_e^{inj}}{4\pi R m_e c^3}, \tag{10}$$

[3] For emission from a spherical region that moves with a Doppler factor δ, the relation between the luminosity as measured in the rest-frame L' and the observed frame L_{obs} is $L_{obs} = \delta^4 L'$.

where $L_{\rm e}^{\rm inj}$ is the total injection luminosity of electrons. Using the relation between Q_0 and $\ell_{\rm e}^{\rm inj}$ for monoenergetic injection, i.e.

$$Q_0 = \frac{3\ell_{\rm e}^{\rm inj} c}{\sigma_{\rm T} R^2 \gamma_0} \tag{11}$$

we find

$$k_{\rm e} = \frac{3}{8\sigma_{\rm T} R\gamma_0}\left(-1+\sqrt{1+\frac{12\ell_{\rm e}^{\rm inj}}{\ell_B}}\right), \tag{12}$$

where the so-called magnetic compactness $\ell_B = \sigma_{\rm T} R u_b$ was introduced. There are two limiting cases that can be studied depending on the value of the ratio $12\ell_{\rm e}^{\rm inj}/\ell_B$:

- synchrotron dominated cooling or $\ell_{\rm e}^{\rm inj} \ll \ell_B/12$, where we find

$$k_{\rm e} \approx \frac{9\ell_{\rm e}^{\rm inj}}{4\sigma_{\rm T}^2 R^2 u_b \gamma_0} + O\left((\ell_{\rm e}^{\rm inj}/\ell_B)^2\right), \tag{13}$$

- and Compton dominated cooling or $\ell_{\rm e}^{\rm inj} \gg \ell_B/12$, where we find

$$k_{\rm e} \approx \frac{3}{4}\left(\frac{3\ell_{\rm e}^{\rm inj}}{R^3\sigma_{\rm T}^3 u_b \gamma_0^2}\right)^{1/2}. \tag{14}$$

2.2. Peak luminosities

The relation between the electron injection rate and the normalization of the distribution at the steady state (Eqs. (9) or (12)) is crucial for the correct calculation of the peak luminosities. The calculation is complete when the proper expressions of the emissivities and of the energies where the peaks appear are taken into account. Our results, for each emission component, are presented below.

Synchrotron component

In the optically thin to synchrotron self-absorption regime, which is the case considered here, the differential synchrotron luminosity per unit volume is given by $J_{\rm syn}(\epsilon) = (c/R)\, u_{\rm s}(\epsilon)$; we note that the units of $J_{\rm syn}$ are erg cm^{-3} s^{-1} per dimensionless energy ϵ. Under the δ-function approximation for the synchrotron emissivity, the peak luminosity (per unit volume) of the corresponding component ($\mathcal{L}_{\rm peak}^{\rm syn}$) emerges at $\epsilon_{\rm peak}^{\rm syn} = b\gamma_0^2$ and is given by

$$\mathcal{L}_{\rm peak}^{\rm syn} \equiv \epsilon J_{\rm syn}(\epsilon)|_{\epsilon=\epsilon_{\rm peak}^{\rm syn}} = \frac{2}{3}\sigma_{\rm T} m_{\rm e} c^3 u_b \gamma_0 k_{\rm e}, \tag{15}$$

or using Eq. (12),

$$\mathcal{L}_{\rm peak}^{\rm syn} = \frac{u_b m_{\rm e} c^3}{4R}\left(-1+\sqrt{1+\frac{12\ell_{\rm e}^{\rm inj}}{\ell_B}}\right). \tag{16}$$

We note that if we were to use the full expression for the synchrotron emissivity (e.g. Rybicki & Lightman 1979), the peak in a νF_ν plot would appear at a slightly different energy than $b\gamma_0^2$.

First SSC component

For parameter values related to the spectral fitting of Cen A, e.g. for $\gamma_0 = 10^3$ and $b \sim 10^{-13}$, we find $\gamma_0\epsilon_{\rm peak}^{\rm syn} = b\gamma_0^3 \ll 1$, i.e. scatterings between the maximum energy electrons with the whole synchrotron photon distribution occur in the Thomson regime. Under the above assumption, the peak luminosity (per unit volume) of the first SSC component ($\mathcal{L}_{\rm peak}^{\rm ssc,1}$) emerges at

$$\epsilon_{\rm peak}^{\rm ssc,1} = \begin{cases} \frac{4}{3} b\gamma_0^4 {\rm e}^{-\frac{1}{1-\alpha}} & \text{for } p<3 \\ \frac{4}{3} b\gamma_0^2\gamma_{\rm c}^2 {\rm e}^{-\frac{1}{1-\alpha}} & \text{for } p>3, \end{cases} \tag{17}$$

where $\alpha = (p-1)/2$ is the synchrotron spectral index and p is the power-law index of the electron distribution at the steady state (see e.g. Gould 1979). In our case the energy of the peak is given by the first branch of the above equation since $p = 2$. The peak luminosity is then given by

$$\mathcal{L}_{\rm peak}^{\rm ssc,1} \equiv \epsilon_1 J_{\rm ssc,1}(\epsilon_1)|_{\epsilon_1=\epsilon_{\rm peak}^{\rm ssc,1}} = \frac{c}{4\pi R} m_{\rm e} c^2 \epsilon_1^2 n_{\rm ssc}^{(1)}(\epsilon_1), \tag{18}$$

where $n_{\rm ssc}^{(1)}$ is the differential number density of SSC photons (1st generation) that is given by

$$n_{\rm ssc}^{(1)}(\epsilon_1) = \frac{4\pi R}{c}\frac{3\sigma_{\rm T} c}{4}\int_{\epsilon_{\rm min}}^{\epsilon_{\rm max}} {\rm d}\epsilon \frac{n_{\rm s}(\epsilon)}{\epsilon} I_{\rm e}(\epsilon_1,\epsilon), \tag{19}$$

where

$$I_{\rm e}(\epsilon_1,\epsilon) = \int_{\max[\gamma_{\rm c},1/2\sqrt{\epsilon_1/\epsilon}]}^{\min[\gamma_0,1/2\sqrt{\epsilon_1/\epsilon}]} {\rm d}\gamma \frac{n_{\rm e}(\gamma)}{\gamma^2} F_{\rm C}(q,\Gamma_{\rm e}). \tag{20}$$

Here $F_{\rm C}(q,\Gamma_{\rm e})$ is the Compton kernel

$$F_{\rm C} = 2q\ln q + (1+2q)(1-q) + \frac{1}{2}\frac{(\Gamma_{\rm e} q)^2}{1+\Gamma_{\rm e} q}(1-q) \tag{21}$$

and

$$\Gamma_{\rm e} = 4\epsilon\gamma \text{ and } q = \frac{\epsilon_1/\gamma}{\Gamma_{\rm e}(1-\epsilon_1/\gamma)}. \tag{22}$$

In the Thomson limit, which therefore applies in our case, $\Gamma_{\rm e} \ll 1$ and $\epsilon_1/\gamma \ll 1$; the Compton kernel takes then the simplified form

$$F_{\rm C} \approx \left(2\frac{\epsilon_1}{4\gamma^2\epsilon}\ln\left(\frac{\epsilon_1}{4\gamma^2\epsilon}\right) + \frac{\epsilon_1}{4\gamma^2\epsilon} + 1 - 2\left(\frac{\epsilon_1}{4\gamma^2\epsilon}\right)^2\right). \tag{23}$$

Following Blumenthal & Gould (1970, hereafter BG70) we assume that the energies of the scattered photons lie away from the high- and low-energy cutoffs. Since the integrand of $I_{\rm e}$ is a steep function of γ, the upper cutoff does not contribute to the integration, and $I_{\rm e}$ is written as

$$\begin{aligned} I_{\rm e} &= \frac{1}{2}k_{\rm e}\left(\frac{\epsilon_1}{4\epsilon}\right)^{-3/2}\int_0^1 {\rm d}y y^{1/2}\left(2y\ln y + y + 1 - 2y^2\right) \\ &= 4k_{\rm e}\left(\frac{\epsilon_1}{\epsilon}\right)^{-3/2} C_1, \end{aligned} \tag{24}$$

where $y = \frac{\epsilon_1}{4\gamma^2\epsilon}$ and $C_1 = 0.975 \simeq 1$. The above expression is then inserted in Eq. (19) and we find

$$n_{\rm ssc}^{(1)}(\epsilon_1) = 8\pi R^2\sigma_{\rm T}^2 k_{\rm e}^2 u_b b^{-1/2} C_1 \ln\Sigma_1 \epsilon_1^{-3/2}, \tag{25}$$

for $4b\gamma_{\rm c}^4 < \epsilon_1 < 4b\gamma_0^4$. In the above, $\ln\Sigma_1$ is the Compton logarithm which also depends on ϵ_1. In reality, $\ln\Sigma_1$ changes

functional form at $\epsilon_\star = \frac{4}{3} b\gamma_0^2\gamma_c^2$, but for the case studied here ($p = 2$) the departure of $n_{\rm ssc}^{(1)}$ from a pure power law with index $-3/2$, at least away from the cutoffs, is not significant (see also Eqs. (27), (28) in Gould 1979). Inserting the above expression into Eq. (18) we find

$$\mathcal{L}_{\rm peak}^{\rm ssc,1} = \frac{3\sqrt{3}}{16e}\frac{u_b m_e c^3}{R}\left(-1+\sqrt{1+\frac{12\ell_e^{\rm inj}}{\ell_B}}\right)^2, \quad (26)$$

where we have neglected the factor $C_1 \ln\Sigma_1$. Whether our choice is justified or not will be tested later on by comparing Eq. (26) against the results obtained with the numerical code.

Second SSC component

As already mentioned in the introduction, in the case of blazars, higher order scatterings (i.e. between electrons and SSC photons of the first generation) are negligible (see e.g. Bloom & Marscher 1996). On the other hand, SSC modelling of SEDs from radio galaxies requires, in general, high electron compactnesses ($\ell_e^{\rm inj}$) because of the deamplified radiation; of course, this is a qualitative argument since the determination of $\ell_e^{\rm inj}$ also depends on the absolute value of the observed flux, the ratio of the peak luminosities of the low- and high-energy humps, and the size of the emitting region. Here we proceed to calculate analytically the peak luminosity of the second SSC component, which will then be compared to the synchrotron and first SSC peak luminosities.

An analogous calculation to that of Eq. (19) for the second generation of SSC photons is, in principle, more complicated because of the Klein-Nishina effects, which for the parameters considered here, become unavoidable. In fact, the scatterings of electrons with SSC photons from the first generation occur only partially in the Thomson and Klein-Nishina regimes. Thus, one must use the full expression of the Compton kernel (e.g. Eq. (2.48) in BG70), which hinders any further analytical calculations. In order to proceed, however, we used a simplified version of the single electron Compton emissivity

$$j_{\rm ssc,2}(\epsilon_2) = j_0\delta\left(\epsilon_2-\frac{4}{3}\gamma^2\epsilon_1\right)H\left(\frac{3}{4}-\gamma\epsilon_1\right), \quad (27)$$

where the step-function introduces an abrupt cutoff in order to approximate the Klein-Nishina suppression and $j_0 = 4/3\sigma_{\rm T} c\gamma^2 u_{\rm ssc,1}$. Here $u_{\rm ssc,1} = m_e c^2\int {\rm d}\epsilon_1\epsilon_1 n_{\rm ssc}^{(1)}$ and $n_{\rm ssc}^{(1)}$ is approximated by a single power law, i.e. it is given by Eq. (25) without the logarithmic term. The differential luminosity of the second SSC component (per unit volume) is then simply

$$J_{\rm ssc,2} = \frac{4}{3}\sigma_{\rm T} c\int_{\gamma_c}^{\gamma_{\rm max}}{\rm d}\gamma\int_{\epsilon_{\rm min}^{\rm ssc,1}}^{\epsilon_{\rm max}^{\rm ssc,1}}{\rm d}\epsilon_1\, I_1(\epsilon_2,\epsilon_1,\gamma), \quad (28)$$

where

$$I_1 = \gamma^2 n_e(\gamma) u_{\rm ssc,1}(\epsilon_1)\delta\left(\epsilon_2-\frac{4}{3}\gamma^2\epsilon_1\right)H\left(\frac{3}{4}-\gamma\epsilon_1\right). \quad (29)$$

After making the integration over γ we find

$$J_{\rm ssc,2} = \frac{\sigma_{\rm T} c}{\sqrt{3}} u_{\rm ssc,1}^0 k_e \epsilon_2^{-1/2} I_2(\epsilon_2), \quad (30)$$

where

$$I_2 = \int_{\epsilon_{\rm min}^{\rm ssc,1}}^{\epsilon_{\rm max}^{\rm ssc,1}}{\rm d}\epsilon_1\frac{1}{\epsilon_1}H\left(\epsilon_2-4/3\gamma_c^2\epsilon_1\right)H\left(E_{\rm min}-\epsilon_2\right). \quad (31)$$

Here $E_{\rm min} = \min[3/4\epsilon_1, 4/3\gamma_0^2\epsilon_1]$, $\epsilon_{\rm min}^{\rm ssc,1} = 4/3 b\gamma_c^4$, $\epsilon_{\rm max}^{\rm ssc,1} = 4/3 b\gamma_0^4$, and

$$u_{\rm ssc,1}^0 = 8\pi m_e c^2 R^2\sigma_{\rm T}^2 u_b b^{-1/2} k_e^2. \quad (32)$$

The integral of Eq. (31) results in the logarithmic term $\ln\Sigma_2$, where Σ_2 is the ratio of the effective upper and lower limits of the first SSC photon distribution, which do not, in principle, coincide with the actual cutoffs. For the purposes of the present study, however, we will neglect the contribution of the logarithmic term. In most cases, the scatterings that result in the second SSC photon generation are only partially in the Klein-Nishina regime and the quantity $\epsilon_2 J_{\rm ssc,2}$ peaks at $\epsilon_{\rm peak}^{\rm ssc,2} = \gamma_0 {\rm e}^{-\frac{1}{1-\alpha_1}}$, where α_1 is the spectral index of the first SSC component and is equal to 1/2 in our work (details on the calculation of the SSC peak in different scattering regimes can be found in LM13). Thus, the peak luminosity $\mathcal{L}_{\rm peak}^{\rm ssc,2}$ is given by

$$\begin{aligned}\mathcal{L}_{\rm peak}^{\rm ssc,2} &\equiv \epsilon_2 J_{\rm ssc,2}(\epsilon_2)|_{\epsilon_2=\epsilon_{\rm peak}^{\rm ssc,2}} \quad (33)\\ &= \frac{8\pi}{\sqrt{3}e} m_e c^3 R^2\sigma_{\rm T}^3 u_b b^{-1/2}\gamma_0^{1/2} k_e^3\end{aligned}$$

or after replacing k_e

$$\mathcal{L}_{\rm peak}^{\rm ssc,2} = \frac{9\sqrt{3}m_e c^3}{64e}\frac{u_b}{b^{1/2}R\gamma_0^{5/2}}\left(-1+\sqrt{1+\frac{12\ell_e^{\rm inj}}{\ell_B}}\right)^3. \quad (34)$$

Finally, using Eqs. (26) and (34) we define the ratio ζ as

$$\zeta \equiv \frac{\mathcal{L}_{\rm peak}^{\rm ssc,2}}{\mathcal{L}_{\rm peak}^{\rm ssc,1}} = \frac{3}{4b^{1/2}\gamma_0^{5/2}}\left(-1+\sqrt{1+\frac{12\ell_e^{\rm inj}}{\ell_B}}\right). \quad (35)$$

In general, if $\zeta > 1$ the system can be led to the so-called Compton catastrophe, where the peak luminosity of the nth–SSC generation is larger than that of the previous one. This succession ceases, however, because of Klein-Nishina effects, as in our case. If the electron cooling is synchrotron dominated ($\ell_e^{\rm inj} \ll 8.3\times10^{-2}\ell_B$), we find $\zeta > 1$ if $\ell_e^{\rm inj} > 8.3\gamma_{0,3}^{5/2}R_{15}^{-1/4}\ell_B^{5/4}$, where we used the notation $Q_x \equiv Q/10^x$ in cgs units. In this regime, both constraints on $\ell_e^{\rm inj}$ cannot be satisfied simultaneously for typical values of γ_0 and R, thus making the Compton catastrophe not relevant. Instead, in the Compton cooling regime ($\ell_e^{\rm inj} > 8.3\times10^{-2}\ell_B$), ζ becomes larger than unity if $\ell_e^{\rm inj} > 570\gamma_{0,3}^5 R_{15}^{-1/2}\ell_B^{3/2}$.

2.3. Tests

In this section we will compare the analytical expressions given by Eqs. (16), (26), and (34) with those obtained from the numerical code described in Mastichiadis & Kirk (1995, 1997), where we have used the full expression for the synchrotron and Compton emissivities (cf. Eqs. (6.33) and (2.48) in Rybicki & Lightman 1979 and BG70, respectively).

For the comparison we used $B = 4$ G, $R = 10^{17}$ cm, $\gamma_0 = 10^3$, and three indicative values of the electron injection compactness, i.e. $\ell_e^{\rm inj} = 10^{-4}, 10^{-3}$, and 10^{-2}. Our results are summarized in Table 1, where the first and second value in each row correspond to the numerical and analytical values, respectively; the ratio ζ given by Eq. (35) is also shown. The magnetic compactness for the parameters used here is $\ell_B = 0.052$. The first

Table 1. Peak luminosities (in logarithm) of the synchrotron, first and second SSC components, along with the ratio ζ of the two SSC peak luminosities.

ℓ_e^{inj}	$\log \mathcal{L}_{peak}^{syn}$	$\log \mathcal{L}_{peak}^{ssc,1}$	$\log \mathcal{L}_{peak}^{ssc,2}$	ζ
10^{-4}	−4.16 (N)	−6.63	−9.64	9.1×10^{-4}
	−3.85 (A)	−6.10	−9.20	
10^{-3}	−3.16	−4.65	−6.66	8.6×10^{-3}
	−2.85	−4.13	−6.20	
10^{-2}	−2.22	−2.77	−3.84	6.5×10^{-2}
	−1.97	−2.40	−3.60	

Notes. In each row the numerical (N) and analytical (A) values are shown as the first and second values, respectively.

two examples fall into the synchrotron dominated regime since $12\ell_e^{inj}/\ell_B = 2.3 \times 10^{-2}$ and 2.3×10^{-1} for $\ell_e^{inj} = 10^{-4}$ and 10^{-3}, respectively. Even though electrons cool preferentially through the ICS of synchrotron photons for the highest ℓ_e^{inj} considered here, we still find $\zeta < 1$.

We note that in all cases the differences between our estimates and the numerically derived values are of a factor of 2–3. In particular, our approximation for the position of the synchrotron peak (see Sect. 2.2) is the main cause for the differences that appear in the first column of Table 1. In general however, our approximations used for the derivation of Eqs. (16), (26), and (34) are reasonable, even in the third case of $\ell_e^{inj} = 10^{-2}$, where $u_{ssc,1} \approx 4(u_B + u_s)$; we note that our analysis neglects the energy density of SSC photons in the electron cooling.

3. One-zone SSC fit to the core emission of Cen A

The emission from the core of Cen A has the double-peaked shape observed in many blazars with the low- and high-energy humps peaking at the infrared and sub-MeV energy ranges, respectively (Jourdain et al. 1993; Chiaberge et al. 2001). The one-zone SSC model, where relativistic electrons are responsible for the radiation observed in low and high energies has been successfully applied over the years to various blazars and recently to FRI galaxies such as M87 (Abdo et al. 2009b). Although it is also the dominant interpretation for the core emission of Cen A, it cannot explain the observed SED up to the TeV energy range (Abdo et al. 2010a; Roustazadeh & Böttcher 2011), since the emitting region is compact enough for signifant absorption of TeV γ-rays on the infrared photons produced inside the source (Abdo et al. 2010a; Sahakyan et al. 2013). We also note that before the detection of Cen A at VHE γ-rays, its whole SED was successfully reproduced by one-zone SSC models (Chiaberge et al. 2001).

In this section we attempt a similar application to the MW emission of Cen A, but we keep in mind that the second SSC photon generation emerges in the SED for (i) high enough electron injection compactnesses; (ii) small size of the emitting region; and (iii) relatively low Lorentz factor of electrons[4] (see also Eqs. (16), (26), and (34)). We also note that the combination of the low electron Lorentz factor with weak magnetic fields, as is often used in SSC models, implies that the second generation Compton scatterings occur only partially in the Thomson regime. For this reason, the second SSC component is expected to be much steeper than the first one.

Under the assumption of monoenergetic electron injection there are five parameters that must be determined in the context of a one-zone SSC model: B, R, δ, γ_0, and ℓ_e^{inj}; for power-law and broken power-law injection the unkwnown parameters increase to seven and nine, respectively (see e.g. Mastichiadis & Kirk 1997; Aleksić et al. 2012). Because there were no detections of variability in the HE/VHE regimes, there are only four available observational constraints: (i) the ratio of the observed peak frequencies $\nu_{peak}^{ssc,1}/\nu_{peak}^{syn}$; (ii) the peak synchrotron frequency $\nu_{peak}^{syn} = 3.2 \times 10^{13}$ Hz; (iii) the ratio of the observed peak fluxes $\left(\nu F_\nu^{syn}\right)_{peak} / \left(\nu F_\nu^{ssc,1}\right)_{peak}$; and (iv) the synchrotron peak flux $\left(\nu F_\nu^{syn}\right)_{peak} \approx 4 \times 10^{-10}$ erg cm^{-2} s^{-1}. From constraints (i) and (ii) we can determine the injection Lorentz factor of electrons γ_0 and find a relation between the magnetic field strength B and the Doppler factor δ, respectively,

$$\gamma_0 = \sqrt{\frac{3}{4}\frac{\nu_{peak}^{ssc,1}}{\nu_{peak}^{ssc,2}}} = 1.1 \times 10^3 \tag{36}$$

and

$$B = B_{cr}\frac{h\nu_{peak}^{syn}}{\delta\gamma_0^2 m_e c^2} = 8\delta^{-1}\ \mathrm{G}, \tag{37}$$

where we neglected the factor $1+z$ because of the small value of the redshift ($z = 0.00183$). The ratio of the electron to magnetic compactness is determined by constraint (iii) and Eqs. (16) and (26):

$$\frac{\ell_e^{inj}}{\ell_B} = \frac{1}{12}\left[-1 + \left(1 + \frac{4e}{3\sqrt{3}}\frac{\left(\nu F_\nu^{ssc,1}\right)_{peak}}{\left(\nu F_\nu^{syn}\right)_{peak}}\right)^2\right] \simeq 5. \tag{38}$$

Combining constraint (iv) with Eqs. (16), (37), and (38) leads to a relation between R and δ:

$$R \simeq 10^{15}\delta^{-1}\ \mathrm{cm}. \tag{39}$$

Finally, using Eqs. (38) and (39) we find

$$\ell_e^{inj} \simeq 10^{-3}\delta^{-3}. \tag{40}$$

Since the viewing angle of the jet is in the range 15°–80°, the Doppler factor cannot exceed the value of 3.7, whereas values as low as 0.52 have been used in the literature (Roustazadeh & Böttcher 2011). From this point on we will adopt the representative value $\delta = 1$, which for an angle of 30° implies a bulk Lorentz factor $\Gamma = 7$. The derived values ($\gamma_0 = 1.1 \times 10^3$, $B = 8$ G, $R = 10^{15}$ cm, $\ell_e^{inj} = 10^{-3}$, and $\delta = 1$) were then used as stepping stones for a more detailed fit to the SED, where we assumed the injection of a steep power-law electron distribution to better reproduce the photon spectrum above 10^{13} Hz. The parameter values, which are only slightly different from the analytical estimates, are listed in Table 2. The values of the SSC fit by Abdo et al. (2010a) are also listed in the same table for comparison. We note that the parameter that differs the most between their fit and ours is the maximum Lorentz factor of the electrons. Assuming that the fastest acceleration timescale of electrons is set by their gyration timescale, the maximum Lorentz factor is saturated at $\gamma_{sat} \simeq 5 \times 10^7$ owing to synchrotron losses in a magnetic field of 6 G. It is safe, therefore, to assume that $\gamma_{e,max} = 10^6$ (see also

[4] Here we imply monoenergetic injection at γ_0. In the case of steep power-law injection between γ_{min} and γ_{max}, the minimum Lorentz factor of electrons plays the role of γ_0.

Table 2. Parameter values for the one-zone SSC model fit to the SED of Cen A shown in Fig. 1.

Parameter	Model	
	SSC	SSC (Abdo et al. 2010a)
R (cm)	4×10^{15}	3×10^{15}
B (G)	6	6.2
δ	1	1
$\gamma_{e,min}$	1.3×10^3	300
γ_{br}	–	800
$\gamma_{e,max}$	10^6	10^8
$p_{e,1}$	–	1.8
$p_{e,2}$	4.3	4.3
ℓ_e^{inj}	6.3×10^{-3}	8×10^{-3}
ℓ_B	4.6×10^{-3}	3.7×10^{-3}

Notes. For comparison, the respective values of the SSC fit by Abdo et al. (2010a) are also shown.

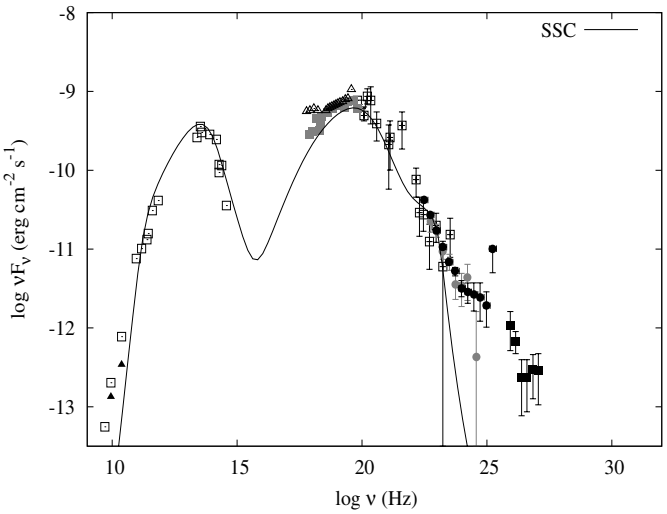

Fig. 1. SED of the core emission from Cen A with a one-zone SSC fit. This includes non-simultaneous observations from low to high frequencies: filled triangles (TANAMI VLBI), grey filled squares (*Suzaku*), open triangles (*Swift*-XRT/*Swift* -BAT), grey circles (1-year *Fermi*-LAT by Abdo et al. 2010a), black circles (4-year *Fermi*-LAT by Sahakyan et al. 2013), black filled squares (H.E.S.S. by Aharonian et al. 2009), and black open squares are archival data from Marconi et al. (2000). The solid line is our one-zone SSC model fit with some slightly different parameters than those used in Abdo et al. (2010a). For the parameters used, see Table 2.

Roustazadeh & Böttcher 2011 for a comment on this point). Our model SED is shown with a solid line in Fig. 1 and a few features of it are worth commenting:

1. The steady-state electron distribution is completely cooled, i.e. $t_{syn}(\gamma_{min}) \ll R/c$. The emission below the peak of the first bump in the SED is attributed to the synchrotron radiation of cooled electrons below γ_{min} and, therefore, it has a spectral index $\alpha = 1/2$. The inverse Compton scatterings of these low-energy synchrotron photons ($x < b\gamma_{min}^2$) with the whole electron distribution occur in the Thomson regime. The resulting spectrum also has an index $\alpha_1 = 1/2$ and it explains fairly well the X-ray data from *Suzaku* and *Swift*.
2. Although the SSC model successfully fits the SED from $\sim 10^{10}$ Hz up to $\sim 10^{23}$ Hz, it fails in the Fermi energy range (grey and black circles in Fig. 1) because of the emergent second SSC photon generation, whose peak appears as a small bump at $\sim 10^{23}$ Hz. In addition, since most of the scatterings occur in the Klein-Nishina regime, the photon spectrum above that bump steepens abruptly.
3. The ratio of the second to the first SSC peak luminosity is ~0.05 as can be seen from Fig. 1. For the parameter values that we derived at the beginning of this section, the analytical expressions given by Eqs. (26) and (34) predict a ratio of ~0.08, which is in good agreement with the numerical value.
4. An attempt to fit the SED using the maximum possible Doppler factor ($\delta = 3.7$) would result in smaller values of R, B, and ℓ_e^{inj} than those listed in Table 2. This would suppress electron cooling, i.e. near/mid-infrared and X-ray observations could not be modelled unless one assumed the injection of a broken power-law electron distribution.

4. Addition of a relativistic proton component

In the previous section we showed that the one-zone SSC model fails to reproduce the core emission of Cen A for energies above a few GeV. A recent analysis of Fermi data from four years of observations resulted in the detection of HE emission up to ~50 GeV (Sahakyan et al. 2013). It is now believed that this part of the spectrum along with the TeV data is produced by a second component that originates either from a compact (sub-pc) or from an extended (~kpc) region. Multiple SSC emitting components (Lenain et al. 2008), non-thermal processes at the black hole magnetosphere (Rieger & Aharonian 2009), photopion and photopair production on background (UV or IR) Kachelrieß et al. (2010) or SSC photons (Sahu et al. 2012), γ-ray induced cascades in a dust torus surrounding the high-energy emitting source (Roustazadeh & Böttcher 2011), non-thermal emission from relativistic protons and electrons that are being injected and accelerated at the base of the jet and cool as they propagate along it (Reynoso et al. 2011) are the proposed scenarios that fall into the first category, whereas scenarios such as inverse Compton scattering of background photons in the kpc-scale jet (Hardcastle & Croston 2011) belong to the second category.

Here we propose an alternative explanation for the TeV and the HE emission in the Fermi energy range, which can be labelled a compact origin scenario. We assume that inside the compact emission region (e.g. $R = 4 \times 10^{15}$ cm) relativistic protons, that have been co-accelerated to high energies along with the electrons, are being injected in the source. In a co-acceleration scenario the ratio of the maximum Lorentz factors achieved by electrons and protons is $\sim m_e/m_p$, as predicted for example by first order Fermi and stochastic acceleration models (see e.g. Rieger et al. 2007). For this reason, and given that $\gamma_{e,max} = 10^6$, we assume that $\gamma_{p,max} = 1.8 \times 10^9$, which does not violate the Hillas criterion since the corresponding gyroradius is $r_g = 4.5 \times 10^{14}$ cm. To reduce the number of free parameters in our model we also assume that the accelerated distributions of protons and electrons have the same power-law index ($p_p = p_e$), although the resulting photon spectrum is insensitive to the exact value p_p.

In order to follow the evolution of a system where both relativistic electrons and protons are being injected with a constant rate in the emitting region, we used the time-dependent numerical code presented in Dimitrakoudis et al. (2012, hereafter DMPR12). The various energy loss mechanisms for the different particle species that are included in our code are

– electrons: synchrotron radiation, inverse Compton scattering;

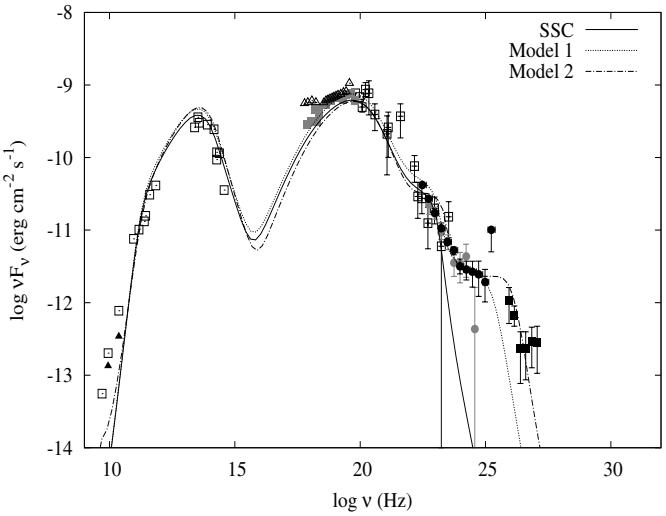

Fig. 2. Leptohadronic fit of the MW core emission of Cen A using the parameter sets shown in Table 3. Models 1 and 2 are shown with dotted and dashed-dotted lines, respectively. For comparison, the one-zone SSC fit shown in Fig. 1 is overplotted with a solid line. All other symbols are the same as in Fig. 1.

- protons: synchrotron radiation, photo-pair (Bethe-Heitler pair production), and photo-pion interactions;
- neutrons: photo-pion interactions, decay into protons;
- photons: photon-photon absorption, synchrotron self-absorption;
- neutrinos: no interactions.

Photohadronic interactions are modelled using the results of Monte Carlo simulations. In particular, for Bethe-Heitler pair production the Monte Carlo results by Protheroe & Johnson (1996) were used (see also Mastichiadis et al. 2005). Photo-pion interactions were incorporated in the time-dependent code by using the results of the Monte Carlo event generator SOPHIA (Mücke et al. 2000).

4.1. Photon emission

As a starting template for the parameters describing the primary leptonic component, we first used the one presented in Table 2. We then added five more parameters that describe the relativistic proton component in order to fit the HE/VHE emission; we refer to this as Model 1. The main difference between Models 1 and 2 is the value of the Doppler factor, which is assumed to be higher in the second model. Subsequently, as already stated in point (4) of the previous section, this affects the values of other parameters such as the electron injection luminosity. The parameters we used for our model SEDs shown in Fig. 2 are listed in Table 3. In general, the addition of a relativistic proton component successfully explains the HE emission detected by the Fermi satellite in both of our models. However, the TeV emission detected by H.E.S.S. can be satisfactorily explained only by Model 2. A zoom in the γ-ray energy range of the SED along with the model spectra is shown in Fig. 3. In what follows, we will first discuss the common features of Models 1 and 2 and, then, we will comment on their differences.

In both models, γ-ray emission is attributed to the synchrotron radiation from secondary electrons produced via Bethe-Heitler pair production and photopion interactions and to the π^0 decay. The hardening of the spectrum at $E \sim 0.4$ GeV, in both cases, is caused by photon-photon absorption. This also explains

Table 3. Parameter values used for our model SED shown in Fig. 2.

Parameter	Model 1	Model 2
R (cm)	4×10^{15}	2.2×10^{15}
B (G)	6	3.5
$t_{\rm cr}$	1.3×10^5 s	7.3×10^4 s
δ	1	2
Γ	7	7
θ	35°	20°
$t_{\rm e,esc}/t_{\rm cr}$	1	4
$\gamma_{\rm e,min}$	1.3×10^3	1.3×10^3
$\gamma_{\rm e,max}$	10^6	10^6
$p_{\rm e}$	4.3	4.5
$\ell_{\rm e}^{\rm inj}$	6.3×10^{-3}	7.9×10^{-4}
$t_{\rm p,esc}/t_{\rm cr}$	1	5
$\gamma_{\rm p,min}$	2×10^7	2×10^7
$\gamma_{\rm p,max}$ [a]	1.8×10^9	1.8×10^9
$p_{\rm p}$	4.3	4.5
$\ell_{\rm p}^{\rm inj}$	4×10^{-6}	7.9×10^{-7}
$u_{\rm r}$ (erg/cm^3) [b]	12.3	2.6
$u_{\rm e}$ (erg/cm^3)	1.9	2.3
$u_{\rm p}$ (erg/cm^3)	6.8	15.4
u_B (erg/cm^3)	1.4	0.5
$L_{\rm e}^{\rm inj}$(erg/s) [c]	1.2×10^{43}	1.3×10^{43}
$L_{\rm p}^{\rm inj}$ (erg/s)	1.4×10^{43}	2.4×10^{43}
$L_{\rm r}$ (erg/s)	2.5×10^{43}	2.5×10^{43}

Notes. [a] Here $\gamma_{\rm p,max} \simeq \left(m_{\rm p}/m_{\rm e}\right)\gamma_{\rm e,max}$. [b] The energy densities refer to the steady state of the system as measured in the comoving frame. [c] The values refer to observed luminosities.

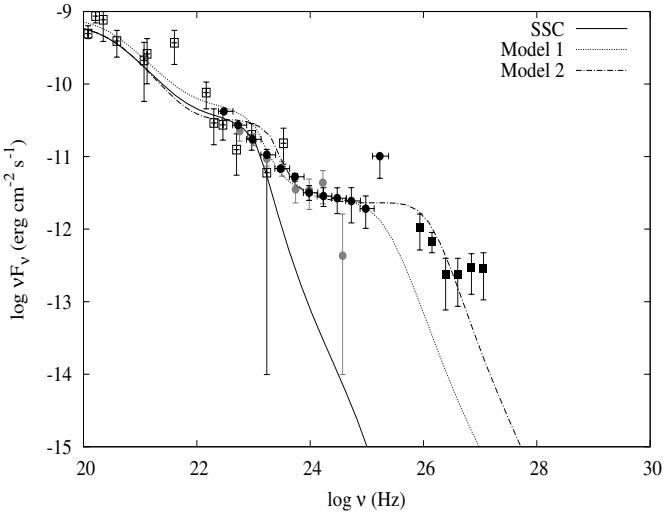

Fig. 3. Zoom of the γ-ray energy range of the MW core spectrum of Cen A. The model spectra are overplotted with different line types marked on the plot.

the weak dependence of the resulting model fit on the slope of the proton distribution.

In the present treatment we consider only the internally produced photons (synchrotron and SSC) as targets for photopair and photopion interactions with the relativistic protons, although external photon fields, such as the radiation from the accretion disk and/or the scattered emission from the broad line region (BLR), could also be important (Atoyan & Dermer 2003). The number density of synchrotron photons scales as

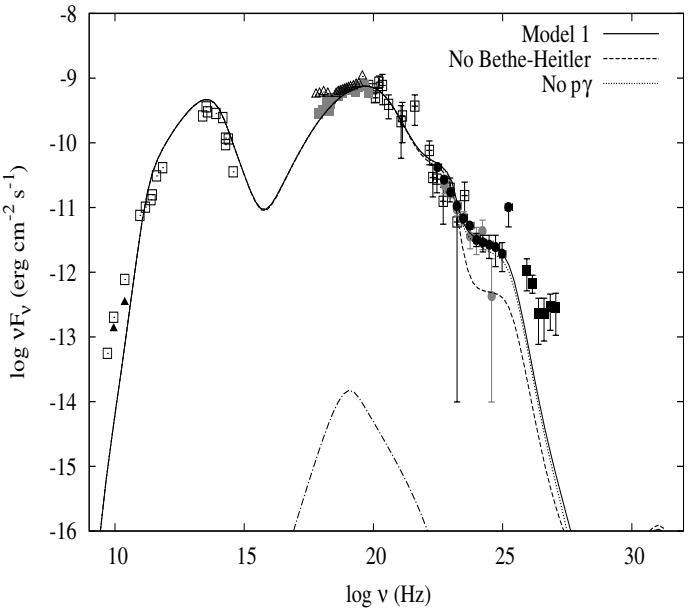

Fig. 4. Contribution of the photohadronic processes to the high-energy part of the spectrum. Our model spectra when all processes are included are shown with a solid line; when photopair and photopion processes are seperately neglected, spectra are shown with dashed and dotted lines, respectively. The dash-dotted curve corresponds to the proton synchrotron emission. For the parameters used see Model 1 in Table 3.

$n_{\rm syn}(\epsilon) \propto \epsilon^{-3/2}$ for $\epsilon^{\rm syn}_{\rm cool} < \epsilon < \epsilon^{\rm syn}_{\rm peak}$, where $\epsilon^{\rm syn}_{\rm cool} \simeq 2.4\times10^{-9}$ and $\epsilon^{\rm syn}_{\rm peak} = 2.4\times10^{-7}$. Thus, protons with Lorentz factors down to $\gamma_{\rm p} \gtrsim 2/\epsilon^{\rm syn}_{\rm peak} \approx 8\times10^{6}$ can interact with this photon field through Bethe-Heitler pair production. Synchrotron photons cannot, however, serve as targets for photopion interactions, since this would require $\gamma_{\rm p}\epsilon^{\rm syn}_{\rm peak} \gtrsim m_\pi/m_{\rm e}$ or equivalently $\gamma_{\rm p} \gtrsim \gamma_{\rm p,max}$. Thus, pion production is solely attributed to interactions of protons with the SSC photon field (see also Sahu et al. 2012). For example, protons with Lorentz factors $\gamma_{\rm p} \gtrsim 1.4\times10^{3}$ and 1.4×10^{7} can interact with the upper ($\epsilon^{\rm ssc,1}_{\rm max} \approx 0.2$) and lower ($\epsilon^{\rm ssc,1}_{\rm min} \approx 2\times10^{-5}$) cutoff of the SSC photon distribution, respectively. For a fixed proton energy, the efficiency of both photopair and photopion interactions depends on the number density of the target field. For the particular set of parameters, one expects that interactions between the high-energy part of the proton distribution and the low-energy part of the photon fields are more efficient in the production of γ-rays. This is illustrated in Fig. 4, where the emitted spectra of Model 1 are shown when (i) all processes are included (solid line); and when (ii) Bethe-Heitler pair-production (dashed line); and (iii) photopion production (dotted line) are omitted. It becomes evident that the main contribution to the high-energy part of the spectrum comes from the Bethe-Heitler pair production process. Moreover, the proton synchrotron emission is lower by many orders of magnitude than the emission from the other components of hadronic origin (dash-dotted line).

For the values of $\gamma_{\rm p,min}$ and $p_{\rm p}$ used in the fit, the required injection compactness to obtain an observable high-energy emission signature is $\ell^{\rm inj}_{\rm p} = 4\times10^{-6}$ and 7.9×10^{-7} for Models 1 and 2, respectively. This corresponds to observed injection luminosities $L^{\rm inj,o}_{\rm p} \simeq 1.4\times10^{43}$ erg/s and 2.4×10^{43} erg/s for the two models, respectively[5]. For a black hole mass $M_{\rm BH} = 5\times10^{7}\,M_\odot$ (Marconi et al. 2006; Neumayer 2010) the Eddington luminosity is $L_{\rm Edd} = 6.5\times10^{45}\,(M_{\rm BH}/M_\odot)$ erg/s and, therefore, the proton injection luminosity in both models is only a fraction of it, i.e. $L^{\rm inj,o}_{\rm p} = \xi L_{\rm Edd}$ with $\xi \approx 10^{-3}$. We also note that the required luminosity of the relativistic proton component is comparable to that of the leptonic component and, therefore, low compared to the values 10^{47}–10^{48} erg/s that are inferred from typical hadronic modelling of blazars (see e.g. Böttcher et al. 2013). For the chosen parameters the emitting region is particle dominated with $u_{\rm p} + u_{\rm e} \approx \kappa_{\rm i} u_B$, where $\kappa_1 = 6$ and $\kappa_2 = 36$ for Models 1 and 2, respectively. We also note that the radiative efficiency η_γ, which we define as $\eta_\gamma = L_{\rm r}/(L^{\rm inj}_{\rm e} + L^{\rm inj}_{\rm p})$, is high for both models; specifically, the values listed in Table 3 indicate $\eta_{\gamma,1} = 0.98$ and $\eta_{\gamma,2} = 0.68$.

In both models we have used a high value for the minimum proton Lorentz factor, which cannot be explained by any theoretical model of particle injection and acceleration. However, any effort to extend such a steep power-law distribution ($p_{\rm p} = 4.3$–4.5) down to $\gamma_{\rm p} = 1$ is excluded from the energetics. As an indicative example, we used the parameter values of Model 1 listed in Table 3 except for a lower value of the minimum Lorentz factor. To obtain a good fit to the SED for $\gamma_{\rm p,min} = 2\times10^{5}$, the required proton injection luminosity increases by almost three orders of magnitude, i.e. $L^{\rm inj}_{\rm p} = 6\times10^{45}$ erg/s. Since there is no physical reason for such high values of the minimum proton energy, one can interpret it as the break energy of a broken power-law distribution. In this case, the power-law below the break must be rather flat, e.g. $p_{\rm p} = 1.5$–2.0, to avoid excessive proton luminosities. A detailed fit using broken power-law energy spectra lies, however, outside the scope of this work. Since there is no known plausible physical scenario that predicts either high values of $\gamma_{\rm p,min}$ or broken power-law energy spectra with $\Delta p_{\rm p} \geq 2.5$, the sub-Eddington proton luminosities listed in Table 3 can be considered a lower limit of those luminosities retrieved using a more realistic proton distribution.

The most important difference between Models 1 and 2 is the assumed value of the Doppler factor. In Model 1, where we did not allow any Doppler boosting of the emitted radiation ($\delta = 1$), we cannot explain the VHE emission. However, by assuming a slightly higher value for the Doppler factor the intrinsic absorbed spectrum is boosted by a factor of $\sim\delta$ in frequency and of $\sim\delta^3$ in flux, respectively. The boosting effect, when combined with the fact that all other parameter values are of the same order of magnitude as those in Model 1, results in a model spectrum that satisfactorily goes through the H.E.S.S. data points. In the light of the recent analysis of the four-year *Fermi*-LAT data (Sahakyan et al. 2013) that implies a common origin of the HE and VHE emission, we believe that Model 2 describes better the emitting region of the core. We note that the connection between the GeV and TeV emission could not be suggested by the previously available one-year *Fermi*-LAT observations Abdo et al. (2010a; grey circles in Fig. 3).

4.2. Neutrino and UHECR emission

The detailed neutrino spectra (of all flavours) obtained using the numerical code of DMPR12 for both models listed in Table 1

[5] For the calculation we used the definition of the proton injection compactness $\ell^{\rm inj}_{\rm p} = L^{\rm o}_{\rm p,inj}\sigma_{\rm T}/(4\pi R\delta^4 m_{\rm p}c^3)$, where the factor δ^4 takes into account Doppler boosting effects for radiation emitted from a spherical volume.

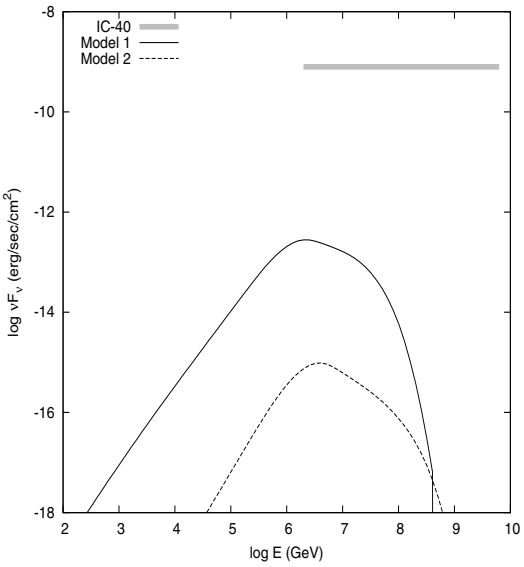

Fig. 5. Neutrino spectra of all flavours as obtained in Models 1 (solid line) and 2 (dashed line) using the numerical code of DMPR12. The thick solid line shows the IC-40 upper limit.

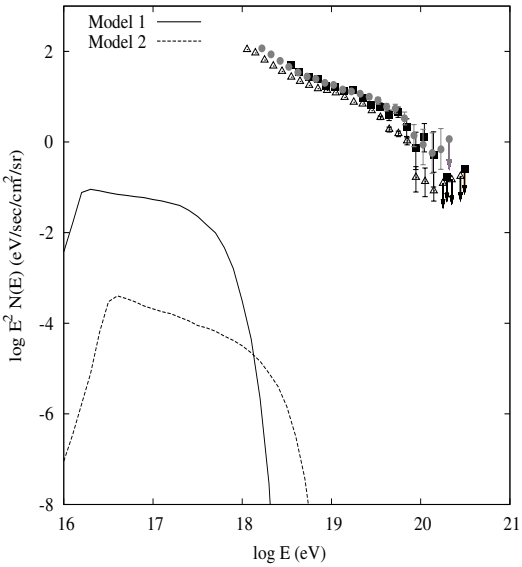

Fig. 6. High-energy proton spectra resulting from the neutron decay as obtained in Models 1 (solid line) and 2 (dashed line) without taking into account the effects of diffusion in the intergalactic magnetic field. The UHECR spectrum as observed by Auger (Abreu et al. 2011), HiRes-I (Abbasi et al. 2009) and Telescope Array (Abu-Zayyad et al. 2013) is overplotted with black open triangles, grey filled circles, and black filled squares, respectively.

are shown in Fig. 5. The neutrino spectra from both models peak at $\sim 10^6$ GeV, while above that energy they can be approximated as power-laws with slopes $p_\nu \sim 1.5$ and ~ 1.6, respectively. This is in agreement with the approximate relation $p_\nu \approx (p_\mathrm{p} - 0.5)/2.5$ derived in DMPR12. The steepening of the spectra above 3×10^7 GeV (Model 1) and 10^8 GeV (Model 2) is due to the cutoff of the proton injection distribution. Although photohadronic processes are significant in modelling the photon spectra above a few GeV, the peak fluxes of neutrinos emitted through the charged pion and muon decay are far below the upper limit of the IceCube 40-string (IC-40) configuration Abbasi et al. (2011, grey line in Fig. 5). The neutrino production efficiency that is defined as $\eta_\nu = L_\nu/(L_\mathrm{e}^\mathrm{inj} + L_\mathrm{p}^\mathrm{inj})$, is approximately 2×10^{-5} and 2×10^{-7} for Models 1 and 2, respectively. Thus, we find that $\eta_\nu \ll \eta_\gamma$, where the radiative efficiency was found to be ~ 0.8. This differentiates the leptohadronic models presented here from others applied to blazar emission, where neutrino efficiencies as high as 0.1 can be obtained (see e.g. Dimitrakoudis et al. 2013 for the case of Mrk 421). In general, there is no case where $\eta_\nu \simeq \eta_\gamma$ (e.g. Reimer 2011) and such low values are to be expected in cases of strong magnetic fields, weak target photon fields, and/or low proton injection compactness; the last applies to our case.

The galaxy Cen A has been under consideration as a potential source of ultra-high-energy cosmic rays (UHECR) from as early as 1978 (Cavallo 1978), and its proximity to our galaxy compared to all other AGN has even inspired models where it is the sole originator of UHECR (Biermann & de Souza 2012). Recently, the *Pierre Auger* Observatory (PAO) has shown an excess in UHECR within 18° of Cen A (Abraham et al. 2007) and, although that region contains a high density of nearby galaxies, further analysis has shown that some of these UHECR may have originated from Cen A itself (Farrar et al. 2013; Kim 2013). For our two models we have obtained distributions for both the escaping protons and neutrons. While the former are susceptible to adiabatic energy losses, and thus any calculation of their flux would constitute an optimistic upper limit, the latter can escape unimpeded and decay into protons well away from the core (Kirk & Mastichiadis 1989; Begelman et al. 1990; Giovanoni & Kazanas 1990; Atoyan & Dermer 2003). In Fig. 6 we have plotted the flux of protons resulting from the decay of neutrons that escape from the emitting region. Since we have not treated cosmic ray (CR) diffusion in the intergalactic magnetic field, which generally decreases the CR flux that arrives at the Earth, our model spectra should be considered only as an upper limit. For both models, the peak fluxes are far lower than the observational limit of PAO. Although that makes the Cen A core an unlikely source of UHECR, these could potentially originate from its lobes instead (e.g. Gopal-Krishna et al. 2010).

5. Summary and discussion

One-zone SSC models for AGN emission have been widely used to fit, with varying degrees of success, the SED of blazars. The discovery of high-energy emission from another class of AGN, i.e. that of radio galaxies, poses new challenges to these models: if radio galaxies are misaligned blazars, then the observed emission should come from a region moving with a relatively large angle with respect to our line-of-sight. This implies a rather small value for the Doppler factor that, for a given flux level of the source, can be compensated only by a large value of the so-called electron compactness parameter.

It is well known that sources with high electron compactness, and consequently high photon compactness, are subject to strong Compton scattering. This usually leads to higher order generations of SSC, while in extreme conditions it might lead to the Compton catastrophe. As clearly these conditions are not apparent in the MW spectra of radio galaxies, one could, by reversing the above arguments, find limits on the parameters used to model the SED of these sources.

As an example, in the present paper we have attempted to fit the SED of the nearby radio galaxy Cen A, that has been observed at GeV and at TeV energies. Most researchers agree that the emitting source is characterized by a low value of the

Doppler factor ($\delta \simeq 1-3$). In order to show the relevance of the first and the second SSC components, in Sect. 2 we have calculated analytically the spectral luminosities at the peaks of these components. Under the assumption that all scatterings producing the first SSC component occur in the Thomson regime, i.e. a condition that can be easily satisfied in most of the relevant cases, we found that the SSC dominates synchrotron cooling whenever $\ell_{\rm e}^{\rm inj} \geq \ell_B/12$, where $\ell_{\rm e}^{\rm inj}$ and ℓ_B are the electron and magnetic compactness, respectively. The calculation of the luminosity of the second SSC component is more complicated as scatterings occur in both the Thomson and Klein-Nishina regimes. However, adopting the common cut-off approximation for the latter, we were able to find a closed expression for the luminosity which, in addition, agrees well with numerical calculations. The same can also be said for the other two components (i.e. synchrotron and first SSC) as can be seen in Table 1.

Using the relations described above as a stepping stone, we have obtained in Sect. 3 a fit to the SED of Cen A. Limiting the Doppler factors by neccessity to small values, we find that the one-zone SSC model can successfully fit the SED up to 10^{23} Hz. At that frequency the peak of the second SSC component appears, which is then followed by a steep power-law segment due to Klein-Nishina effects. This causes, typical one-zone SSC modelling to fail at fitting the high-energy observations of Cen A.

In order to fit the emission at frequencies above 10^{23} Hz, we have introduced, in Sect. 4.1, a hadronic component which, we assume, is co-accelerated to high energies along with the leptonic component. Assuming that the two populations share the same characteristics, i.e. their injection power laws have the same slope and their maximum cutoffs are related to each other through a simple relation stemming from the Fermi acceleration processes, we found that acceptable fits to the SED of Cen A can be obtained for proton injection luminosities of the same order of magnitude as the electron one (see Table 3). Interestingly enough, fits using $\delta = 2$ can attribute the TeV observations to hadronic emission, while fits with $\delta = 1$ fail to do so because of strong photon-photon attenuation.

In Sect. 4.1 we have also shown that $\gamma_{\rm p,min} \gg 1$ in order to obtain the required radiative efficiency of the photohadronic interactions under the assumption of a steep power-law distribution for protons and the requirement of a sub-Eddington proton injection luminosity. On the one hand, such high values of $\gamma_{\rm p,min}$ may be interpreted as the break energy of a broken-power law at injection. On the other hand, one could, in principle, reconcile the hypothetical low values of $\gamma_{\rm p,min}$ and the high values of $L_{\rm p}^{\rm inj}$ by also considering external photon fields, such as diffuse and/or line emission from the BLR, as targets for photohadronic interactions. In the case of Cen A, however, the lack of strong broad emission lines implies that these photon fields are negligible (Alexander et al. 1999; Chiaberge et al. 2001). Another possible photon target field could be the mid-IR radiation that is believed to be associated with cool dust in the nuclear region of Cen A (e.g. Karovska et al. 2003). For the observed fluxes, which range from 1 to 100 Jy (Israel 1998; Karovska et al. 2003), the number density of mid-IR photons as measured in the rest frame of the high-energy emitting region is many orders of magnitude lower than that of the internally produced synchrotron photons. Thus, incorporating the IR photon field in the calculations presented here would not lower the requirement of high proton luminosities.

The consideration of relativistic protons in the emitting region is inevitably related to the neutrino emission, since proton interactions with the photon fields present in the source result in charged meson production. In Sect. 4.2 we have presented the neutrino spectra calculated for both our models. For the employed parameters the efficiency of pion production is very low and this can also be seen at the low peak neutrino fluxes which are many orders of magnitude below the IceCube upper limit.

Furthermore, high-energy neutrons resulting from photopion interactions are an effective means of facilitating proton escape from the system, as they are unaffected by its magnetic field and their decay time is long enough to allow them to escape freely before reverting to protons (e.g. Kirk & Mastichiadis 1989; Begelman et al. 1990). Another advantage is that they are unaffected by adiabatic energy losses that the protons may sustain in the system as it expands (Rachen & Mészáros 1998). These effects make them excellent candidates for UHE protons. For our model parameters, i.e. steep injection proton spectra and small values of the Doppler factor, the obtained proton distributions peak in the range $10^{16}-10^{17}$ eV, where the effects of CR diffusion in the intergalactic magnetic field cannot be neglected. Since in the present work we have not treated CR diffusion, our results should be considered an upper limit. Still, these are well below the observed CR flux at these energies. In the light of recent results suggesting Cen A to be the origin of some UHECR events observed by PAO (Farrar et al. 2013; Kim 2013) and of our model results, the core of Cen A cannot be the production site of UHECR.

Our analysis has shown that Cen A can be explained by means of a leptohadronic model as was the case of Mrk 421 (Mastichiadis et al. 2013). However, unlike that source, a one-zone SSC model fails to reproduce the SED of Cen A mainly because of complications arising from the appearance of the second SSC component. Although this feature has been overlooked by many researchers, it may play a crucial role in fitting the SEDs of radio galaxies, as these require high electron luminosities, making the conditions very favourable for its appearance.

Acknowledgements. We would like to thank the referee Dr. Markus Böttcher for his suggestions and for pointing out several misprints in the manuscript. This research has been co-financed by the European Union (European Social Fund – ESF) and Greek national funds through the Operational Program "Education and Lifelong Learning" of the National Strategic Reference Framework (NSRF) – Research Funding Program: Heracleitus II. Investing in knowledge society through the European Social Fund. E.L. acknowledges financial support from the *Thales* project 383549 that is jointly funded by the European Union and the Greek Government in the framework of the programme "Education and lifelong learning".

References

Abbasi, R. U., Abu-Zayyad, T., Al-Seady, M., et al. (High Resolution Fly's Eye Collaboration) 2009, Astropart. Phys., 32, 53
Abbasi, R., Abdou, Y., Abu-Zayyad, T., et al. 2011, ApJ, 732, 18
Abdo, A. A., Ackermann, M., Ajello, M., et al. 2009a, ApJ, 699, 31
Abdo, A. A., Ackermann, M., Ajello, M., et al. 2009b, ApJ, 707, 55
Abdo, A. A., Ackermann, M., Ajello, M., et al. 2010a, ApJ, 719, 1433
Abdo, A. A., Ackermann, M., Ajello, M., et al. 2010b, Science, 328, 725
Abraham, J., Abreu, P., et al. (Pierre Auger Collaboration) 2007, Science, 318, 938
Abreu, P., Aglietta, M., et al. (Pierre Auger Collaboration) 2011 [arXiv:1107.4809]
Abu-Zayyad, T., Aida, R., Allen, M., et al. 2013, ApJ, 768, L1
Aharonian, F., Akhperjanian, A. G., Anton, G., et al. 2009, ApJ, 695, L40
Aleksić, J., Alvarez, E. A., Antonelli, L. A., et al. 2012, A&A, 542, A100
Alexander, D. M., Hough, J. H., Young, S., et al. 1999, MNRAS, 303, L17
Atoyan, A. M., & Dermer, C. D. 2003, ApJ, 586, 79
Begelman, M. C., Rudak, B., & Sikora, M. 1990, ApJ, 362, 38
Begelman, M. C., Fabian, A. C., & Rees, M. J. 2008, MNRAS, 384, L19

Biermann, P. L., & de Souza, V. 2012, ApJ, 746, 72
Bloom, S. D., & Marscher, A. P. 1996, ApJ, 461, 657
Blumenthal, G. R., & Gould, R. J. 1970, Rev. Mod. Phys., 42, 237
Böttcher, M., & Chiang, J. 2002, ApJ, 581, 127
Böttcher, M., Reimer, A., & Marscher, A. P. 2009, ApJ, 703, 1168
Böttcher, M., Reimer, A., Sweeney, K., & Prakash, A. 2013, ApJ, 768, 54
Cavallo, G. 1978, A&A, 65, 415
Celotti, A., & Ghisellini, G. 2008, MNRAS, 385, 283
Chiaberge, M., Capetti, A., & Celotti, A. 2001, MNRAS, 324, L33
Costamante, L., Aharonian, F., Buehler, R., et al. 2009 [arXiv:0907.3966]
Dimitrakoudis, S., Mastichiadis, A., Protheroe, R. J., & Reimer, A. 2012, A&A, 546, A120
Dimitrakoudis, S., Petropoulou, M., & Mastichiadis, A. 2013, Astropart. Phys., submitted
Fanaroff, B. L., & Riley, J. M. 1974, MNRAS, 167, 31P
Farrar, G. R., Jansson, R., Feain, I. J., & Gaensler, B. M. 2013, JCAP, 1, 23
Ferrarese, L., Mould, J. R., Stetson, P. B., et al. 2007, ApJ, 654, 186
Ghisellini, G., Celotti, A., Fossati, G., Maraschi, L., & Comastri, A. 1998, MNRAS, 301, 451
Giannios, D., Uzdensky, D. A., & Begelman, M. C. 2010, MNRAS, 402, 1649
Giovanoni, P. M., & Kazanas, D. 1990, Nature, 345, 319
Gopal-Krishna, Biermann, P. L., de Souza, V., & Wiita, P. J. 2010, ApJ, 720, L155
Gould, R. J. 1979, A&A, 76, 306
Hardcastle, M. J., & Croston, J. H. 2011, MNRAS, 415, 133
Hardcastle, M. J., Worrall, D. M., Kraft, R. P., et al. 2003, ApJ, 593, 169
Harris, G. L. H., Rejkuba, M., & Harris, W. E. 2010, PASA, 27, 457
Hartman, R. C., Bertsch, D. L., Bloom, S. D., et al. 1999, ApJS, 123, 79
Israel, F. P. 1998, A&ARv, 8, 237
Jourdain, E., Bassani, L., Roques, J. P., et al. 1993, ApJ, 412, 586
Kachelrieß, M., Ostapchenko, S., & Tomàs, R. 2010, PASA, 27, 482
Karovska, M., Marengo, M., Elvis, M., et al. 2003, ApJ, 598, L91
Kim, H. B. 2013, ApJ, 764, 121
Kirk, J. G., & Mastichiadis, A. 1989, A&A, 213, 75
Konopelko, A., Mastichiadis, A., Kirk, J., de Jager, O. C., & Stecker, F. W. 2003, ApJ, 597, 851
Lenain, J.-P., Boisson, C., Sol, H., & Katarzyński, K. 2008, A&A, 478, 111
Majaess, D. 2010, Acta Astron., 60, 121
Marconi, A., Schreier, E. J., Koekemoer, A., et al. 2000, ApJ, 528, 276
Marconi, A., Pastorini, G., Pacini, F., et al. 2006, A&A, 448, 921
Mastichiadis, A., & Kirk, J. G. 1995, A&A, 295, 613
Mastichiadis, A., & Kirk, J. G. 1997, A&A, 320, 19
Mastichiadis, A., Protheroe, R. J., & Kirk, J. G. 2005, A&A, 433, 765
Mastichiadis, A., Petropoulou, M., & Dimitrakoudis, S. 2013, MNRAS, 434, 2684
Morganti, R., Fosbury, R. A. E., Hook, R. N., Robinson, A., & Tsvetanov, Z. 1992, MNRAS, 256, 1P
Mücke, A., Engel, R., Rachen, J. P., Protheroe, R. J., & Stanev, T. 2000, Comput. Phys. Commun., 124, 290
Neumayer, N. 2010, PASA, 27, 449
Padovani, P., & Urry, C. M. 1990, ApJ, 356, 75
Padovani, P., & Urry, C. M. 1991, ApJ, 368, 373
Protheroe, R. J., & Johnson, P. A. 1996, Astropart. Phys., 4, 253
Rachen, J. P., & Mészáros, P. 1998, Phys. Rev. D, 58, 123005
Reimer, A. 2011, in AGN Physics in the CTA Era, PoS (AGN 2011) 006
Reynoso, M. M., Medina, M. C., & Romero, G. E. 2011, A&A, 531, A30
Rieger, F. M., & Aharonian, F. A. 2009, A&A, 506, L41
Rieger, F. M., Bosch-Ramon, V., & Duffy, P. 2007, Ap&SS, 309, 119
Roustazadeh, P., & Böttcher, M. 2011, ApJ, 728, 134
Rybicki, G. B., & Lightman, A. P. 1979, Radiative processes in astrophysics (New York: Wiley Interscience)
Sahakyan, N., Yang, R., Aharonian, F. A., & Rieger, F. M. 2013, ApJ, 770, L6
Sahu, S., Zhang, B., & Fraija, N. 2012, Phys. Rev. D, 85, 043012
Tingay, S. J., Jauncey, D. L., Reynolds, J. E., et al. 1998, AJ, 115, 960
Yang, R.-Z., Sahakyan, N., Wilhelmi, E. D. O., Aharonian, F., & Rieger, F. 2012, in AIP Conf. Ser. 1505, eds. F. A. Aharonian, W. Hofmann, & F. M. Rieger, 590